ORIGINAL PAPER

Multiscale modeling of human bone

Y. W. Kwon[1] · B. R. Clumpner[1]

Abstract

A multiscale modeling technique was developed to predict mechanical properties of human bone, which utilizes the hierarchies of human bone in different length scales from nanoscale to macroscale. Bone has a unique structure displaying high stiffness with minimal weight. This is achieved through a hierarchy of complex geometries composed of three major materials: hydroxyapatite, collagen and water. The identifiable hierarchical structures of bone are hydroxyapatite, tropocollagen, fibril, fiber, lamellar layer, trabecular bone, cancellous bone and cortical bone. A helical spring model was used to represent the stiffness of collagen. A unit cell-based micromechanics model computed both the normal and shear stiffness of fibrils, fibers, and lamellar layers. A laminated composite model was applied to cortical and trabecular bone, while a simplified finite element model for the tetrakaidecahedral shape was used to evaluate cancellous bone. Modeling bone from nanoscale components to macroscale structures allows the influence of each structure to be assessed. It was found that the distribution of hydroxyapatite within the tropocollagen matrix at the fibril level influences the macroscale properties significantly. Additionally, the multiscale analysis model can vary any parameter of any hierarchical level to determine its effect on the bone property. With so little known about the detailed structure of nanoscale and microscale bone, a model encompassing the complete hierarchy of bone can be used to help validate assumptions or hypotheses about those structures.

Keywords Multiscale model · Biomaterial · Bone

1 Introduction

Biomaterials are living tissues that have developed through evolutionary processes. They are distinct for their complex hierarchies built by simple materials (Vaughan et al. 2012). There are a limited number of structural materials in the human body, but living organisms rely on composite hierarchical structures to achieve macroscale forms and functions (Cui et al. 2007). Biomaterials such as skin, ligaments, tendons, muscles and bones exhibit this hierarchical organization. This study focuses on the structure of bone.

Bone is the main structural component of the body. Unlike tendons and ligaments, bone structures support both tensile and compressive loads, as well as bending, torsional and shearing loads (Hench and Jones 2005). To understand and predict the structural properties of bone, a multiscale model is presented. This model begins at the nanoscale level and continues up the hierarchies to the macroscale level. The hierarchical structure of the bone is sketched in Fig. 1. To the authors' best knowledge, no attempt has been undertaken to link the material properties in the nanoscale to those in the macroscale. Almost all previous studies investigated material properties in a single length scale, especially at the macroscale. Reviews on previous studies are discussed later when appropriate to be introduced.

The multiscale analysis model is presented in the following section, adhering to the hierarchical order as shown in Fig. 1. Then, the predicted results at each length scale model are compared to available data, if any, to validate the model in the subsequent section. Finally, conclusions are provided.
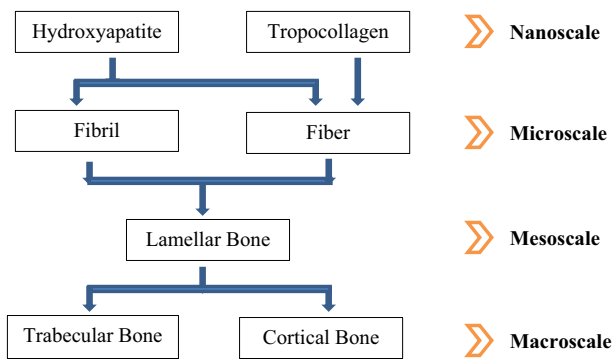
2 Multiscale analysis

2.1 Nanoscale model

Human bone consists of hydroxyapatite (HA), tropocollagen (TC), water and others. Among them, hydroxyapatite and tropocollagen are the major load-bearing components.

✉ Y. W. Kwon
    ywkwon@nps.edu

[1] Department of Mechanical and Aerospace Engineering,
    Naval Postgraduate School, Monterey, CA 93940, USA

Fig. 1 Hierarchical structures of bone from nanoscale to microscale

Hydroxyapatite has a large surface area to volume ratio, allowing for rapid absorption and dissolution when ions are needed (Buschow et al. 2001; Cui et al. 2007). Furthermore, the HA structures are organized into small plates ranging from 1.5 to 5 nm thick (Rho et al. 1998). Although the size of HA crystals varies based on location, mineral density and time allowed for growth; the average crystal size is considered as 50 nm × 25 nm × 3 nm (Nikolaeva et al. 2007; Buehler 2006). The crystal lattice of HA has the hexagonal close packed structure. From the nanoindentation testing completed on single HA crystals, the stiffness in the [0001] direction was 150 GPa, while the stiffness in the [1010] direction was 143 GPa (Zamiri and De 2011).

The tropocollagen molecule is the basic molecular unit of collagen. There are 28 different variations of collagen; each is used for a different physiological purpose within the body (Ricard-Blum 2011). Collagen I is the main collagen species found in bone, comprising 95% of the total collagen (Tzaphlidou and Berillis 2005). Collagen I is composed of three helical protein strands: two alpha-1 type-1 strands and one alpha-1 type-2 strand (Hench and Jones 2005). The polyproline-II (PPII) helices of the alpha-1 type-1 and alpha-1 type-2 collagen contain a common repeating subunit: Gly-X-Y. The combination of the alpha-1 type-1 and alpha-1 type-2 helices creates the right handed triple helix of the TC molecule.

To determine the quantitative values for each tropocollagen triple helix, a helical spring model is used. It is assumed that each repeating subunit of the polyproline helices is represented by Gly-Pro-Hyp. A helical spring is used to assess the stiffness of a single molecule of tropocollagen, because each left-handed polyproline helix of the TC molecule can be independently treated as a spring. Buckling is prevented through stabilizing hydrogen bonds, van der Waals attraction and the close packing of the TC molecules within collagen fibrils. The stiffness of a single TC molecule is equal to the stiffness of the combined alpha-1 type-1 and alpha-1 type-2 strands.

The spring constant of each helix is computed from the following equation

$$k = \frac{F}{y} = \frac{Gd^4}{8D^3 N_A} \tag{1}$$

where k and G are the spring constant and the shear modulus, d and D are the wire and mean coil diameter, and N_A is the number of coils. Typical values for the TC model (Hamed and Jasiuk 2013; Reznikov et al. 2014) are $G = 67.9$ GPa, $d = 0.286$ nm, $D = 0.5$ nm, and $N_A = 300$. The shear modulus was the most difficult to estimate, since no data is available for the shear modulus of a single chain amino acid helix. To create a valid estimate, the bond energy of the backbone of a single subunit was calculated. The shear modulus of the TC backbone is computed as energy over volume, which equates to 67.9 GPa. The calculation above neglects all strengthening effects of cross-linking, non-backbone atoms and other atomistic considerations, but still provides a basic starting point to calculate the overall stiffness of collagen.

Finally, the elastic modulus of TC is computed from

$$E = 3 \left(\frac{L}{A} \right) k \tag{2}$$

where L and A are the length and cross-sectional area of the helix spring, and the factor 3 comes from the sum of the three helices. For the TC helix, the length is 300 nm, and the area equals to $\pi D^2 / 4$.

2.2 Microscale model

A micromechanical unit cell model (Kwon and Kim 1998; Kwon and Park 2013; Park and Kwon 2013; Kwon and Darcy 2018) is used to compute microscale bone properties. This model is a rectangular prism divided into 8 subcells, as shown in Fig. 2. Each subcell may have a different material, and the unit cell model computes the effective material properties of all subcells such as elastic moduli, Poisson's ratios and coefficients of thermal expansion in every axis. The details of the unit cell model were given in the references (Kwon and Kim 1998; Kwon and Park 2013; Park and Kwon 2013; Kwon and Darcy 2018). As a result, only a brief summary of the model is provided here.

Uniform stresses and strains are assumed for each subcell as shown in Fig. 2. Subcell stresses must satisfy the equilibrium at their interfaces. For example, subcells #1 and #2 should maintain the following equilibrium:

$$\sigma_{11}^1 = \sigma_{11}^2$$
$$\sigma_{12}^1 = \sigma_{12}^2$$
$$\sigma_{13}^1 = \sigma_{13}^2 \tag{3}$$

where σ_{ij}^k denotes the stress tensor. The subscripts indicate stress components according to the axes shown in Fig. 2, and
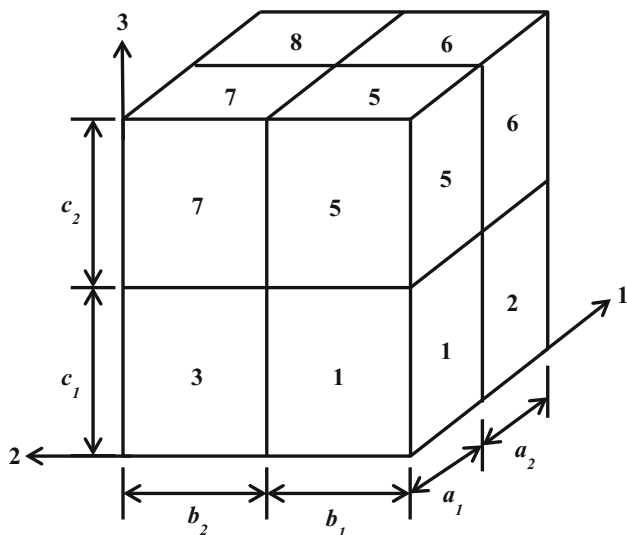
Fig. 2 Unit cell of micromechanics model

the superscripts indicate subcell number. The similar set of equilibrium equations are applied to all subcell interfaces.

In addition to stress equilibrium, deformation compatibility must be met for the unit cell. Deformation compatibility, for instance along the 1-axis, results in the following equations:

$$
\begin{aligned}
a_1\varepsilon_{11}^1 + a_2\varepsilon_{11}^2 &= a_1\varepsilon_{11}^3 + a_2\varepsilon_{11}^4 \\
&= a_1\varepsilon_{11}^5 + a_2\varepsilon_{11}^6 \\
&= a_1\varepsilon_{11}^7 + a_2\varepsilon_{11}^8
\end{aligned}
\tag{4}
$$

in which ε_{ij}^k is the strain tensor whose indices are defined in the same way as those for the stress tensor. Similar equations can be developed for the deformation compatibility along other axes as well as for the shear deformation.

Furthermore, each subcell has a constitutive equation defining strain.

$$
\varepsilon_{ij}^n = C_{ijkl}^n \sigma_{kl}^n + \alpha_{ij}^n \Delta\theta
\tag{5}
$$

For this model, the thermal expansion of the materials is ignored. This can be assumed because the internal temperature of the human body is highly regulated.

The total unit cell stress and strain, denoted with an overbar, can then be found by averaging the subcell stresses and strains based on the subcell volumes.

$$
\overline{\sigma}_{ij} = \sum_{n=1}^{8} V^n \sigma_{ij}^n
\tag{6}
$$

$$
\overline{\varepsilon}_{ij} = \sum_{n=1}^{8} V^n \varepsilon_{ij}^n
\tag{7}
$$

Combining all the equations discussed above can yield the following equation:

$$
[T]\{\varepsilon\} = \{f\}
\tag{8}
$$

If the normal and shear components are not coupled together, the normal and shear components can be solved independently. In the present case, each subcell is considered as either isotropic or orthotropic. Therefore, there is no coupling between the normal and shear components. Then, the matrix $[T]$ is a 24×24 matrix for the normal components, because each subcell has three normal strain components. A similar matrix equation can be written for the shear components. Here, only the normal components are discussed, because the same derivation can be applied to the shear components.

The vector $\{f\}$ is a 24×1 column vector composed of a 21×1 column containing zeros, representing the stress and strain equilibrium, and a 3×1 column containing the effective normal strains.

$$
\{f\}^T = [[0] \ [\overline{\varepsilon}_{11} \ \overline{\varepsilon}_{22} \ \overline{\varepsilon}_{33}]]
\tag{9}
$$

Solving Eq. (8) produces the following expression.

$$
\{\varepsilon\} = [T]^{-1}\{f\}
\tag{10}
$$

The inverse of $[T]$ can be further broken down into three matrices. These are substituted into Eq. (10) to obtain the following.

$$
[T]^{-1} = [[R1][R2][R3]]
\tag{11}
$$

$$
\{\varepsilon\} = [R3][\overline{\varepsilon}_{11} \ \overline{\varepsilon}_{22} \ \overline{\varepsilon}_{33}]^{-1}
\tag{12}
$$

Furthermore, Eq. (6) can be written as:

$$
\{\overline{\sigma}\} = [V]\{\sigma\}
\tag{13}
$$

which finally results in the following expression:

$$
\{\overline{\sigma}\} = [V]([E]\{\varepsilon\}) = [V][E][R3]\{\overline{\varepsilon}\}
\tag{14}
$$

where $[E]$ is a matrix of the inverse of the subcell compliance tensors stated in Eq. (5). Then, the unit cell stiffness can be calculated.

$$
[\overline{E}] = [V][E][R3]
\tag{15}
$$

The $[\overline{E}]$ matrix is the 3×3 matrix of the unit cell stiffness. With these values, the Poisson's ratio of the unit cell can also be found.

(a)

(b)
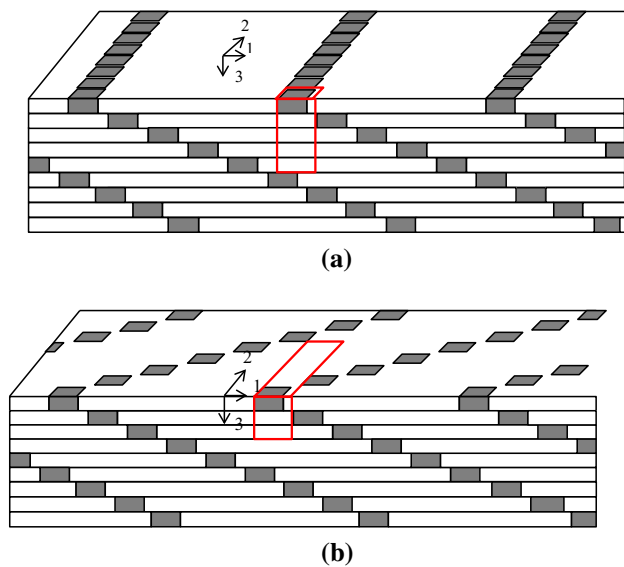
Fig. 3 Repeated unit cell selected for fibril models: **a** linear and **b** twist models

2.2.1 Fibril model

The fibril is the smallest microstructure of the bone. It is represented by a staggered array of HA crystals and TC molecules. The regular organization of fibrils is caused by fibrillogenesis. The crystals for the fibrillar models have a length of 50 nm, a width of 25 nm, and a height of 3 nm. The linear packing model is a lateral repeat of the fibril array as shown in Fig. 3a. A small section is repeated throughout the array in 67 nm increments. The repeated unit cell is selected for the linear fibril model in the figure. The dimensions of the unit cell have $a_1 = 50$ nm, $a_2 = 17$ nm, $b_1 = 25$ nm, $b_2 = 3$ nm, $c_1 = 3$ nm, and $c_2 = 9$ nm.

For many years, a linear fibril orientation has been the accepted model (Nikolaeva et al. 2007). This model was viewed as a long thin filament with alternating bands of mineral rich phase and mineral deficient phase. Although the linear model presents a viable solution, there has not been any evidence proving lateral growth is a purely linear process. Fibrils grow laterally in 4 nm steps by electrostatic attraction during the formation of the microscale fibril (Gibson 1994). A twisting crystalline structure was more recently considered for fibril model. The 67 nm periodicity, which determined the two-dimensional stacking, was assumed to direct the three-dimensional pattern. For this reason, the lateral periodicity is also 67 nm. A simplified twisted model is shown in Fig. 3b.

The twisting fibril takes into account a 67 nm periodicity in the 2 direction as well as the 3 direction. Additionally, because each repeated stack in the 2 direction contains the same 67 nm periodicity in the 3 direction, the subunit is shortened in the 3 direction. The repeated unit cell for the twisting fibril model is shown in Fig. 3b. The dimensions associ-

(b)
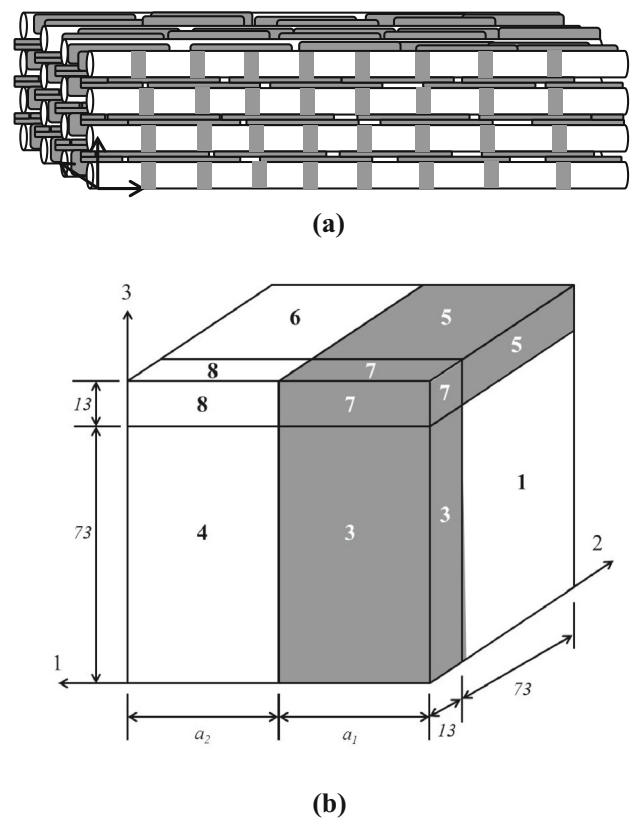
Fig. 4 **a** Sketch of fiber and **b** unit cell applied to the fiber model. Dark subcells 3, 5, and 7 represents minerals attached to the fibril denoted by subcells 1 and 6. The remaining subcells are filled with water or void depending on compression or tension, respectively

ated with the twisting model are $a_1 = 50$ nm, $a_2 = 17$ nm, $b_1 = 25$ nm, $b_2 = 75$ nm, $c_1 = 3$ nm, and $c_2 = 6$ nm. For both fibril models, subcell #1 in Fig. 2 is assigned HA properties; the remaining subcells are assigned TC properties.

2.2.2 Fiber model

The subsequent hierarchy following the bone fibril is that of the bone fiber. Fibers consist of fibrils and HA. The HA is present in the fibers, as both extrafibrillar mineral deposited between densely packed fibrils and intrafibrillar mineral within each fibril (Vaughan et al. 2012; Rho et al. 1998). Each closely packed fibril is surrounded by a crust of mineral, approximately 20–30 nm thick, where the long axis of minerals and fibrils run parallel to each other (Gautieri et al. 2013). The thickness of the crust is estimated as 26 nm. Additionally, the diameter of a single uniform fibril is assumed to be 150 nm (Rho et al. 1998). This three-dimensional structure is shown in Fig. 4a with the surface mineral removed.

The fibers found in the micro level are single bundles of fibrils or a combination of many bundles: each bundle is an organized and repeating arrangement of fibrils and HA. Accordingly, the unit cell micromechanics model is aptly

Table 1 Dimension for fiber unit cell with extrafibrillar mineralization

%EFM	a_1	a_2
50	0.50	0.50
70	0.70	0.30
90	0.90	0.10
95	0.95	0.05

suited for modeling bone fiber, as the fiber unit cell relies on volume fractions of each material.

This area percent of the subcell #1 face in Fig. 2 assumes a total crust thickness of 26 nm and a fibril diameter of 150 nm. When symmetry is applied, a crust of 13 nm and a radius of 75 nm are utilized. These dimensions are applied to the micromechanics unit cell model with $b_1 = 75$ nm, $b_2 = 13$ nm, $c_1 = 75$ nm, and $c_2 = 13$ nm. To test the effect of fibril mineralization, the degree of mineralization is varied, which is denoted as %EFM and defined as the total percent of the fibril surface covered by minerals. In Fig. 4b, subcells 3, 5, and 7 represent the minerals covering the fibril. Therefore, by altering the length of a_1, %EFM is varied for the fiber. We assume that the fiber is comprised of no more than 95% EFM. The different levels of mineralization analyzed are listed in Table 1. In compression, subcells 4, 6, and 8 in Fig. 4b are assigned the properties of water. In tension, these subcells are assigned as void spaces.

2.3 Macroscale model

2.3.1 Lamellar bone

The next hierarchical step of bone is that of lamellar bone. Lamellar bone is a fiber reinforced composite of bone fibers and bone fibrils. The lamellar bone model utilizes the knowledge that fibers within a lamellar layer are unidirectional and that the disordered matrix has a relatively random thickness, within the bounds defined by (Gautieri et al. 2013). Figure 5 shows the simplified view of lamellar layers. The macroscale model used for the lamellar layers assumes that the layer thickness is 2.5 μm and the matrix thickness is 0.375 μm. The longitudinal cross-section of the micromechanics model provides a 38.4% fiber volume for the lamellar unit cell. The presence of the small pores is neglected, as they account for approximately 0.1% of the current model's volume and they are not uniformly present along the length of the fibers.

To model the lamellar layer as a continuous fiber, the material properties assigned to subcells #1, #3, #5 and #7 in Fig. 2 are mirrored for subcells #2, #4, #6 and #8. This produces a continuous fiber reinforced composite. The dimensionless values to be used for this model are $a_1 = 0.5$, $a_2 = 0.5$, $b_1 = 0.62$, $b_2 = 0.38$, $c_1 = 0.62$, and $c_2 = 0.38$.

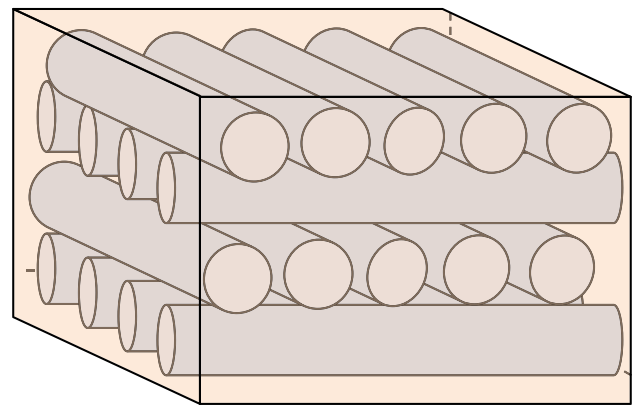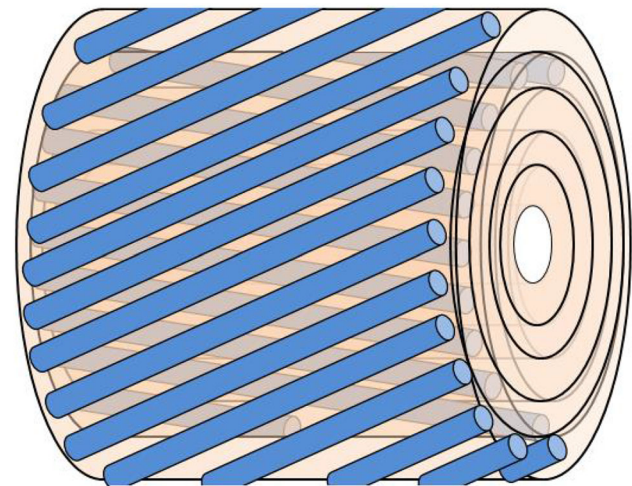**Fig. 5** Simplified model for lamellar bone

Fig. 6 Simplified model for cortical bone

The material properties of a single lamellar layer in a different fiber orientation can be found by rotating the layer with respect to the 3-axis. This rotation can be completed by rotating the stiffness matrix of the material (Gibson 1994).

2.3.2 Cortical bone

Cortical bone is composed of concentric layers of lamellar bone, known as osteons. Osteons can be made of primary or secondary bone. Secondary osteons are called Haversian systems, which are analyzed in this study. The concentric layers composing Haversian systems form a cylindrical structure approximately 200 μm in diameter (Reznikov et al. 2014) as shown in Fig. 6. Each concentric layer associated with the osteon is composed of lamellar bone. The fibers of each individual layer are unidirectional in alignment. The center cylinder is representative of a Haversian canal and will be represented as un-bound water. Multiple Haversian systems are packed together in cortical bone. Due to their circular shape, there are incomplete layers at the interface of each Haver-

Table 2 Preferential orientation of layered composite model

Layer	Fiber orientation (°)	Volume fraction
Transverse	72.5	0.45
Longitudinal	22.5	0.35
Intermediate	0	0.05
Intermediate	40	0.05
Intermediate	55	0.05
Intermediate	90	0.05

Table 3 Fiber orientation of trabecular bone layer model

Fiber direction	Volume fraction
−10°	0.20
−5°	0.20
0°	0.20
5°	0.20
10°	0.20

sian system where the boundaries intersect. These boundaries are defined by a cement line, which is an identifiable region where osteon growth direction has transitioned. The properties of cement lines are similar to those of the surrounding bone, despite the misnomer of 'cement' (Skedros et al. 2005).

The fiber directions of the concentric lamellar layers vary for each layer. Two distinct patterns have been identified in lamellar bone: a periodic alternating pattern and a continuous fiber twist. The two models for cortical bone rely on the volume percent of a defined fiber orientation. The preferential model has the fiber orientations as listed in Table 2. On the other hand, the smooth model assumes even distribution of fibers at 10° intervals. The fiber directions as stated by (Skedros et al. 2005; Harley et al. 1997) do not designate either positive or negative angles about the longitudinal axis. Therefore, it is assumed that the fiber orientations are equal in both positive and negative angles for the cortical bone model to produce an orthotropic linear elastic material. In addition, due to the random radial distribution of osteons, the cortical bone is expected to have a transverse isotropic material.

2.3.3 Trabecular bone

Trabecular bone is the term used in this paper to classify the material contained within single trabeculae of cancellous bone. Cancellous bone is the term used to identify the macroscale structure of all interlocking trabeculae. Trabecular bone is more metabolically active than cortical bone. The deposition of new bone is related to the applied stresses on the cancellous bone (Reznikov et al. 2014). Trabecular bone is modeled using the same layered composite model as utilized for cortical bone. However, the fiber orientations and volume percent of each layer are altered. The fiber orientations and their volume percent in trabecular bone are listed in Table 3. Due to the lack of Haversian canals in trabecular bone, the void space is a result of microscopic canaliculi. This void space is evaluated at 5% volume percent and is treated as a liquid in compression and a void in tension.
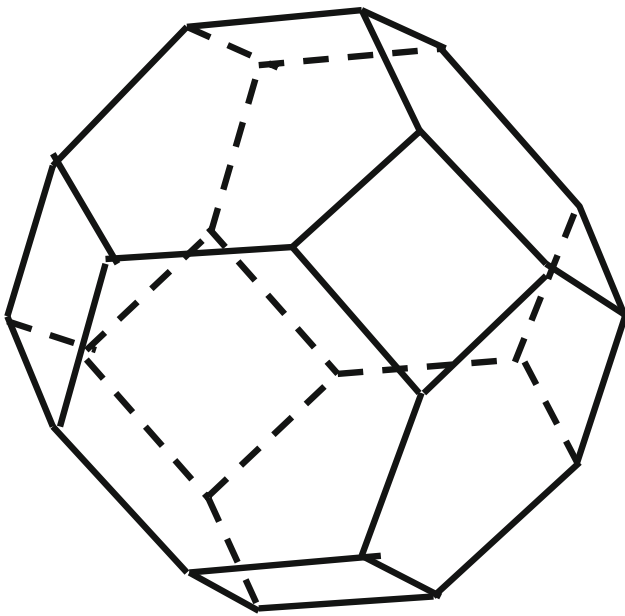
2.3.4 Cancellous bone

While a laminated composite material represents the material properties of a single trabecula, it does not quantify the properties of cancellous bone. The structure of cancellous bone is a uniquely three-dimensional problem, that cannot be solved through a two dimensional approximation (Odgaard 1997). Additionally, there is much heterogeneity in cancellous bone at different anatomical locations (Parkinson and Fazzalari 2013).

Early models of cancellous bone utilized a model of rods and plates. Four early models were an asymmetric rod-like cubic model, a plate-like cubic model, a rod-like hexagonal columnar model, and a plate-like hexagonal columnar model (Gibson 1985). These early models helped to shape simple models of cancellous bone. However, these models provided asymmetrical properties for cancellous bone. Additionally, the early models included Euler buckling as a failure mechanism. Later experiments have shown that failure of cancellous bone is most commonly due to microscopic cracking, which removes buckling as a failure mode for trabeculae (Fyhrie and Schaffler 1994).

Complex finite element models have been used to model cancellous bone. Three-dimensional models formed from micro-computed tomography can replicate small sections of bone (Kadir et al. 2010). Furthermore, two unit cells have been proposed that are able to accurately model cancellous bone. Kadir et al. (2010) compared the results of prismatic unit cells and tetrakaidecahedral unit cells to those of a micro-computed tomography model. The authors found that both unit cells accurately represent the mechanical properties. Additionally, Guo and Kim (2002) have shown that a complex finite element model of several tetrakaidecahedron cells can accurately represent different levels of bone loss due to aging.

This study makes use of a tetrakaidecahedron (TKDH) unit cell to calculate the macroscale properties of cancellous bone as sketched in Fig. 7. Several values of trabecular bone properties are used, as well as different bone densities. The results of the macroscale properties are then compared to experimental data.

Fig. 7 Tetrakaidecahedron for cancellous bone model

Table 4 Material properties of fibril model component

Material	E_L (GPa)	E_T (GPa)	ν	G (GPa)
Hydroxyapatite	150	143	0.23	59.7
Tropocollagen under compression	3.43	3.43	0.35	1.27
Tropocollagen under tension	3.26	3.26	0.35	1.21

The TKDH has eight hexagonal faces, six square faces, 36 edges and 24 vertices. For the open cell structures present in cancellous bone, the faces are treated as voids and the edges are treated as trabeculae. A simple finite element model was developed by (Kwon et al. 2003) to analyze the TKDH frame. Each ligament in the TKDH geometry is modeled as a 3-D beam which has the property of the trabecula. The details of the 3-D beam element are shown in (Kwon et al. 2003) and it is omitted here to save space.

3 Results and discussion

3.1 Nanoscale result

To compute the elastic modulus of the tropocollagen, the geometric and material properties as discussed in the previous section are used for Eq. (1). In addition, the length and diameter of the helix are considered as 300 and 0.7 nm, respectively, for Eq. (2). Then, a single helix has the elastic modulus of 1.18 GPa and TC has three helices with the modulus of 3.54 GPa. The experimental data in (Carter and Caler 1981; Zysset et al. 1999) showed 3.0 and 5.1 GPa. The present value agrees well with the data.

3.2 Microscale result

3.2.1 Fibril

The collagen network is assumed to stagger its array with at least a 25 nm width, so as to allow for the generally accepted

dimensions of the HA crystals. The micromechanical model provides results for both the linear and twisted packing models. For both models, the material properties shown in Table 4 are used. In this and following tables, subscript 'L' denotes the longitudinal direction, while 'T' means the transverse direction.

In addition to using two different models to explore the crystal arrays within fibrils, the presence of water is taken into account with the calculation of material properties. The presence of water produces a bi-modulus composite material, as water is only considered in compression. While the volume percent water is much higher in tendons and ligaments, bone is known to have approximately 10–25% water. Some of this is thought be found within the nanoscale tropocollagen and hydroxyapatite. Water serves as a binding and stabilizing agent within the triple helix of tropocollagen. Additionally, small amounts of water are tightly bound within the HA crystal. However, the rest is assumed be held within the various hierarchies. For the purpose of the fibrillar model, each unit cell is assumed to have 8% volume of water. This is calculated by adjusting the stiffness of collagen to assume an 8% volume of water in compression and an 8% volume of void space in tension. Tropocollagen in compression and tension exhibits the different properties as shown in Table 4.

The resulting values for the fibril models are shown in Table 5. These results can be compared to the experimental transverse modulus between 3.07 ± 0.23 and 7.65 ± 3.85 GPa (Kotha and Guzelsu 2007). The present fibril moduli are close to the experimental data.

One metric for comparing validity of theoretical models is to compare bone mineral content. However, very little information is available as to the mineral content of microstructures. Therefore, the mineral content at each level is tracked for comparison at the macro level. The linear fibril model has 16.7% mineral volume fraction, while the twisting fibril model has 6.2 % mineral volume fraction.

3.2.2 Fiber

The results for the fiber model are calculated both in compression and tension using the geometric data. As expected, due to the applied symmetry, the fiber exhibits transverse

Table 5 Predicted material property of fibril

Model	E_L (GPa)	E_T (GPa)	G_{TT} (GPa)	G_{LT} (GPa)	v_{TL}	v_{TT}
Linear						
Compression	6.05	6.60	1.53	1.68	0.30	0.30
Tension	5.76	6.30	1.46	1.59	0.30	0.30
Twisting						
Compression	4.26	3.81	1.35	1.37	0.31	0.37
Tension	4.05	3.62	1.29	1.30	0.31	0.37

Table 6 Predicted fiber compressive material property

	50% EFM		70% EFM		90% EFM		95% EFM	
	Linear	Twisting	Linear	Twisting	Linear	Twisting	Linear	Twisting
E_L (GPa)	6.51	5.45	7.57	6.51	11.6	10.5	16.2	15.0
E_T (GPa)	16.7	14.6	21.4	19.2	26.4	23.9	27.7	25.2
G_{TT} (GPa)	1.05	0.93	1.47	1.30	1.89	1.67	2.00	1.77
G_{LT} (GPa)	0.01	0.01	0.02	0.02	0.06	0.06	0.11	0.11
v_{TL}	0.37	0.41	0.36	0.40	0.30	0.31	0.25	0.25
v_{TT}	0.14	0.13	0.13	0.12	0.13	0.12	0.13	0.12

Table 7 Estimated mineral volume percent of fiber model

%EFM	Mineral volume fraction (%)	
	Linear	Twisting
50	25.9	18.4
70	31.5	23.9
90	37.0	29.5
95	38.4	30.9

isotropic material properties. Table 6 shows the results for compression.

The results in compression show that the linear fibril model produces a stiffer fiber in all normal and shear cases and in all directions. For all %EFM, the fiber shear modulus G_{LT} is much less than G_{TT}. As %EFM increases from 50 to 95%, the shear modulus G_{LT} increases by an order of magnitude and G_{TT} increases approximately double. This is exhibited for both the linear and the twisting models. The

Poisson's ratio in the transverse plane remains relatively constant, but as %EFM increases, v_{TL} decreases. The results in tension show similar results to those in compression.

The difficulty with evaluating the results of the fiber model is that there is an absence of experimental testing available for comparison. Fibers exist within the macrostructures of bone and are not easily isolated for testing. Additionally, almost all theoretical calculations assume that macrostructure bone is composed solely of layered fibers. However, the macrostructures of bone are fiber reinforced composites with fibrils acting as the matrix and bone fibers as the fibers.

The mineral content completely surrounds the fibril. This complete encirclement increases the normal stiffness in the transverse direction and stiffens the fiber against shear on the transverse plane. The mineral content of the different fiber models was calculated. These calculations include both intrafibrillar and extrafibrillar HA. The resulting values are shown in Table 7.

Table 8 Predicted lamellar compressive material property

	50% EFM		70% EFM		90% EFM		95% EFM	
	Linear	Twisting	Linear	Twisting	Linear	Twisting	Linear	Twisting
E_L (GPa)	6.43	4.61	6.84	5.02	8.39	6.55	10.1	8.27
E_T (GPa)	9.00	6.43	9.72	6.93	10.4	7.41	10.6	7.58
G_{TT} (GPa)	1.34	1.16	1.55	1.34	1.71	1.47	1.74	1.49
G_{LT} (GPa)	0.62	0.53	0.630	0.54	0.67	0.57	0.72	0.62
v_{TL}	0.33	0.37	0.32	0.35	0.28	0.29	0.24	0.24
v_{TT}	0.24	0.27	0.24	0.27	0.24	0.29	0.25	0.30

Table 9 Estimated mineral volume percent of lamellar model

%EFM	Mineral volume fraction (%)	
	Linear	Twisting
50	20.2	10.9
70	22.4	13.0
90	24.5	15.2
95	25.0	15.7

3.3 Macroscale result

The results of the lamellar micromechanics model were calculated in both compression and tension for four different %EFM. The resulting stiffness and Poisson's ratios are shown in Table 8 for compression. Both linear and twisting fibril models were used in the prediction. Through the bone hierarchies, the mineral content of the lamellar layers was calculated. The mineral volume fraction of each model is displayed in Table 9. The mineral volume fraction within lamellar layers is representative of macroscale bone mineral content and comparisons can be made to theoretical and experimental values. Early studies of fibril organization suggested total bone mineral volume content at 50% (Guo and Kim 2002). Calculation of the bone ash content of adult cows was found to be close to 70%. The volume percent of bone ash does not directly correlate to bone mineral content. This method results in a large estimate of mineral content, as additional residues remain from sources other than hydroxyapatite. More recent studies estimate a lower bone mineral volume. Kotha and Guzelsu (2007) postulate that mineral volume content is 40% for bone, while (Ashman and Rho 1988) approximates 33–43% hydroxyapatite mineral volume. These estimates are based on a more complete

understanding of the hierarchical structure of bone, but are still estimates as bone mineral content varies with bone type, anatomical position, age, and gender.

When comparing the bone mineral content from this study to those found through experimental and theoretical methods, the linear crystal pattern emerges as the more viable model. The mineral volume fractions of the twisting model are too low to validate its use. Even with slight perturbations to the constraints applied to the fibril and fiber models, the mineral content of the twisting model does not match the current estimates.

For the subsequent analyses, only the linear fibril model is used. Additionally, the preferential and smooth layered models were calculated in both tension and compression. The compressive results are shown in Table 10. The results of the cortical model can be compared to results from (Buehler 2006) as shown in Table 11.

When compared based on the similar mineral volume content, the present model computes comparable moduli with the finite element results with 20% mineral volume percent as shown in Table 11. Increase in mineral content for different hierarchical models would increase the stiffness of the cortical bone as shown in Table 11.

Furthermore, the results of the trabecular laminated composite model for both compression and tension are shown in Table 12. Table 13 lists the experimental and theoretical results for trabecular bone. The predicted results in Table 12 are comparable to those in Table 13.

The results of the cancellous bone TKDH model were calculated using the trabecular results in compression and tension. These two values were used to create bounds on the stiffness of cancellous bone. The results of the three anatomical locations are shown in Table 14. The present results are comparable to other tested data shown in Table 15.

Table 10 Predicted cortical bone material property under compression

	50% EFM		70% EFM		90% EFM		95% EFM	
	Pref.	Smooth	Pref.	Smooth	Pref.	Smooth	Pref.	Smooth
E_L [GPa]	5.07	4.64	5.39	4.91	5.94	5.45	6.42	5.92
E_T [GPa]	5.84	5.68	6.22	6.05	6.82	6.59	7.28	6.99
G_{TT} [GPa]	0.70	0.74	0.77	0.82	0.84	0.89	0.87	0.92
G_{LT} [GPa]	0.94	0.96	1.04	1.05	1.14	1.16	1.21	1.23
ν_{TL}	0.32	0.36	0.32	0.36	0.31	0.35	0.31	0.34
ν_{TT}	0.23	0.23	0.23	0.22	0.22	0.22	0.22	0.22

Table 11 Published cortical elastic modulus

Elastic modulus (GPa)	Method	Source
6	FEM, 20% mineral volume fraction	Buehler (2006)
9	FEM, 30% mineral volume fraction	
15	FEM, 40% mineral volume fraction	
21	FEM, 50% mineral volume fraction	

Table 12 Predicted trabecular bone property in compression and tension

	50% EFM		70% EFM		90% EFM		95% EFM	
	Comp.	Tens.	Comp.	Tens.	Comp.	Tens.	Comp.	Tens.
E_L (GPa)	6.05	5.10	6.43	5.16	7.85	5.23	9.45	5.25
E_T (GPa)	8.52	7.76	9.19	8.57	9.79	9.13	9.98	9.25
G_{TT} (GPa)	1.26	1.20	1.46	1.39	1.61	1.53	1.64	1.56
G_{LT} (GPa)	0.66	0.62	0.67	0.64	0.72	0.67	0.77	0.72
ν_{TL}	0.24	0.25	0.24	0.26	0.24	0.32	0.24	0.38
ν_{TT}	0.23	0.25	0.23	0.24	0.24	0.24	0.25	0.24

Table 13 Published values for trabecular property

Elastic modulus (GPa)	Method	Source
18.1 ± 1.7	Nanoindentation (transverse)	Kadir et al. (2010)
12.7 ± 2.0	Ultrasound (isotropic)	Yoon and Katz (1976)
3.8	Three-point bending	Cowin and Mehrabadi (1989)
5.4 ± 1.4	Four-point bending	Gong et al. (2010)

Table 14 Predicted cancellous elastic modulus (all expressed in MPa)

	50% EFM		70% EFM		90% EFM		95% EFM	
	Comp.	Tens.	Comp.	Tens.	Comp.	Tens.	Comp.	Tens.
Femoral neck	292	246	311	249	379	252	457	253
Femoral head	196	165	209	167	255	170	307	170
Distal/proximal	300	253	319	256	390	259	469	260

Table 15 Published values for cancellous property

Elastic modulus (MPa)	Method	Source
300	Micro-compression testing	Majumar et al. (1997)
110	Compressive testing	Krug et al. (2008)
550	Mechanical testing	Ding and Hvid (2000)

4 Conclusions

The structures of biomaterials are highly dependent on complex geometries. This study has shown that material properties of hierarchical structures can be found by analyzing each level independently. By linking all hierarchies and adjusting parameters, the influence of each level can then be analyzed. Additionally, changes to the geometry at each level can be completed to test assumptions about the structure of bone.

The nanoscale constituents of bone were described, and a spring model was utilized to calculate the longitudinal stiffness of tropocollagen. This simple model produced accurate results. Additionally, a micromechanical unit cell model was used to analyze the microscale components of bone. Bone fibrils represent a particle reinforced matrix, while bone fibers are a fiber reinforced composite. The fibrillar model produced accurate results as compared to accepted values. The fiber model could not be compared to experimental results, so different variations were carried over to the next hierarchy.

The first macroscale structures of bone are the lamellar layers. These were modeled as a fiber reinforced composite and compared to accepted values of mineral fraction volume. The results disproved the twisting hydroxyapatite fibrillar model. The linear fibril model was utilized for both cortical and trabecular bone. These macroscale structures utilized a layered composite model to calculate their transverse isotropic material properties.

A simple finite element model of a tetrakaidecahedron was used to model cancellous bone. From experimental testing, the volume fractions of bone and trabecular thicknesses were defined for different anatomical locations. The model was shown to accurately predict the properties of cancellous bone.

This model can be used to validate future discoveries about the structure of bone. As technology advances, imaging capabilities will allow the nanostructures of bone to be explored in detail. The discoveries can be checked against this model to assess their impact on macroscale properties. Additionally, the properties of synthetic bone materials can be checked

against the hierarchical structure of bone. This would allow for more anatomically beneficial bone grafts.

Compliance with ethical standards

Conflict of interest On behalf of all authors, the corresponding author states that there is no conflict of interest.

References

Ashman RB, Rho JY (1988) Elastic modulus of trabecular bone material. J Biomech 21(3):177–181

Buehler MJ (2006) Atomistic and continuum modeling of mechanical properties of collagen: elasticity, fracture, and self-assembly. J Mater Res 21(8):1947–1961

Buschow KH, Cahn J, Flemings RW, Ilschner MC, Kramer B, Mahajan EJ (2001) Bone mineralization. In: Encyclopedia of materials science and technology, pp 787–794

Carter DR, Caler WE (1981) Uniaxial fatigue of human cortical bone. The influence of tissue physical characteristics. J Biomech 14(7):461–470

Cowin SC, Mehrabadi MM (1989) Identification of the elastic symmetry of bone and other materials. J Biomech 22(6–7):503–515

Cui FZ, Li Y, Ge J (2007) Self-assembly of mineralized collagen composites. Mater Sci Eng 57:1–27

Ding M, Hvid I (2000) Quantification of age-related changes in the structure model type and trabecular thickness of human tibial cancellous bone. Bone 26(3):291–295

Fyhrie DP, Schaffler MB (1994) Failure mechanisms in human vertebral cancellous bone. Bone 15(1):105–109

Gautieri A, Vesentini S, Redaelli A, Ballarini R (2013) Modeling and measuring visco-elastic properties: From collagen molecules to collagen fibrils. Int J Non-Linear Mech 56:25–33

Gibson LJ (1985) The mechanical behavior of cancellous bone. J Biomech 18(5):317–328

Gibson RF (1994) Principles of composite material mechanics. McGraw-Hill Inc., New York

Gong H, Zhu D, Gao J, Linwei L, Zhang X (2010) Ad adaptation model for trabecular bone at different mechanical levels. BioMed Eng OnLine 9(32):1–17

Guo XE, Kim CH (2002) Mechanical consequence of trabecular bone loss and its treatment: a three-dimensional model simulation. Bone 30(2):404–411

Hamed E, Jasiuk I (2013) Multiscale damage and strength of lamellar bone modeled by cohesive finite elements. J Mech Behav Biomed Mater 28:94–110

Harley R, James D, Miller A, White JW (1997) Phonons and the elastic moduli of collagen and muscle. Nature 267:285–287

Hench LL, Jones JR (2005) Clinical needs and concepts of repair, biomaterials. In: Hench LL, Jones JR (eds) Artificial organs and tissue eng. Sawston, UK, Woodhead, pp 79–89

Kadir MR, Syahrom A, Öchsner A (2010) Finite element analysis of idealised unit cell cancellous structure based on morphological indices of cancellous bone. Med Biol Eng Comput 48:497–505

Kotha SP, Guzelsu N (2007) Tensile behavior of cortical bone: dependence of organic matrix material properties on bone mineral content. J Biomech 40:36–45

Krug R, Carballido-Gamio J, Burhardt AJ, Kazakia G, Hyun BH, Jobke B, Banerjee S, Huber M, Link TM TM, Majumdar S (2008) Assessment of trabecular bone structure comparing magnetic resonance imaging at 3 Tesla with high-resolution peripheral quantitative computed tomography ex vivo and in vivo. Osteoporos Int 19(5):653–661

Kwon YW, Cooke RE, Park C (2003) Representative unit-cell models for open-cell metal foams with or without elastic fillers. Mater Sci Eng A 343:63–70

Kwon YW, Darcy J (2018) Failure criteria for fibrous composites based on multiscale model. Multiscale Multidiscip Model Exp Des 1(1):3–17

Kwon YW, Kim C (1998) Micromechanical model for thermal analysis of particulate and fibrous composites. J Therm Stress 21:21–39

Kwon YW, Park MS (2013) Versatile micromechanics model for multiscale analysis of composite structures. Appl Compos Mater 20(4):673–692

Nikolaeva TI, Tiktopulo EI, Il'yasova EN, Kuznetsova SM (2007) Collagen type I fibril packing in vivo and in vitro. Biophysics 52(5):489–497

Majumar S, Genant HK, Grampp S, Newitt DC, Truong VH, Lin JC, Mathur A (1997) Correlation of trabecular bone structure with age, bone mineral density, and osteoporotic status: in vivo studies in the distal radius using high resolution magnetic resonance imaging. J Bone Miner Res 12(1):111–118

Odgaard A (1997) Three-dimensional methods for quantification of cancellous bone architecture. Bone 20(4):315–328

Park MS, Kwon YW (2013) Elastoplastic micromechanics model for multiscale analysis of metal matrix composite structures. Comput Struct 123:28–38

Parkinson IH, Fazzalari NL (2013) Characterisation of trabecular bone, studies in mechanobiology, tissue engineering and biomaterials, vol 5, pp 31–51

Reznikov N, Shahar R, Weiner S (2014) Bone hierarchical structure in three dimensions. Acta Biomater 10:3815–3826

Rho JY, Kuhn-Spearing L, Zioupos P (1998) Mechanical properties and the hierarchical structure of bone. Med Eng Phys 20:92–102

Ricard-Blum S (2011) The collagen family. Cold Spring Harb Perspect Biol 3(1):a004978

Skedros JG, Holmes JL, Vajda EG, Bloebaum RD (2005) Cement lines of secondary osteons in human bone are not mineral-deficient: New data in a historical perspective. Anat Rec Part 286A(1):781–803

Tzaphlidou M, Berillis P (2005) Collagen fibril diameter in relation to bone site. A quantitative ultrastructural study. Micron 36:703–705

Vaughan TJ, McCarthy CT, McNamara LM (2012) A three-scale finite element investigation into the effects of tissue mineralisation and lamellar organisation in human cortical and trabecular bone. J Mech Behav Biomed Mater 12:50–62

Yoon HS, Katz JL (1976) Ultrasonic wave propagation in human cortical bone-II. Measurements of elastic properties and microhardness. J Biomech 9(7):459–464

Zamiri A, De S (2011) Mechanical properties of hydroxapatite single crystals from nanoindentation data. J Mech Behav Biomed Mater 2(4):146–152

Zysset PK, Guo XE, Hoffler CE, Moore KE, Goldstein SA (1999) Elastic modulus and hardness of cortical and trabecular bone lamellae measured by nanoindentation in the human femur. J Biomech 32(10):1005–1012